Composition Effects in Polymer Blends Spin-Cast on Patterned Substrates

J. Raczkowska,[†] P. Cyganik,[†] A. Budkowski,[*,†] A. Bernasik,[†,‡] J. Rysz,[†] I. Raptis,[§] P. Czuba,[†] and K. Kowalski[‡]

M. Smoluchowski Institute of Physics and Joint Center for Chemical Analysis and Structural Research, Jagellonian University, Reymonta 4, 30-059 Kraków, Poland; Faculty of Physics and Applied Computer Science and Faculty of Metallurgy and Materials Science, AGH−University of Science and Technology, Mickiewicza 39, 30-059 Kraków, Poland; and Institute of Microelectronics, NCRS "Demokritos", 15310 Aghia Paraskevi, Greece

Received June 13, 2005

ABSTRACT: Blends of poly(2-vinylpyridine), polystyrene, and poly(methyl methacrylate) of four different compositions (2:3:0, 3:2:0, 1:1:0, and 2:2:1 w:w:w) were spin-cast onto periodically ($\lambda = 4\ \mu$m) patterned substrate (with two alternating stripes: Au attracting PVP and neutral self-assembled monolayer), and resulting film morphologies (with inherent domain scale $0.2\ \lambda \le R < 1.8\ \lambda$) were recorded with scanning force microscopy and examined with Fourier transform analysis and the integral geometry approach. The morphologies depend on not only spatial (R/λ) but also compositional commensuration between blends and symmetric pattern: $\lambda/2$-substructures are present, in addition to λ-structures, for isolated (2:3:0) but not for continuous (3:2:0) PVP domains. This explains also the data for 1:1:0 blends which present a transition from isolated to continuous PVP domains (for larger R values). In turn, interfacial compatibilizer (PMMA in 2:2:1) results in the well-ordered $\lambda/2$-substructures for both morphology types.

1. Introduction

Simple, low-cost approaches were proposed for multicomponent polymer films, simultaneously allowing for the surface pattern-guided alignment of various (micro)-phase domains, which might form various functional elements of potential hi-tech devices:[1] Long-ranged ordered microphase structures were obtained for symmetric[2] and asymmetric[3] block copolymers positioned on the pattern. In turn, pattern-directed structure formation reported for spin-cast (solvent-quenched)[2,4−9] or temperature-quenched[4,10−13] binary blend films correspond to symmetric (or critical)[10−12] homopolymer mixtures only. This limits domain patterns available for potential applications.[14,15]

Surface pattern replication is controlled by many parameters, mainly by film thickness and the competition between surface and interfacial energy.[16−18] Another important problem is the commensuration between the pattern periodicity λ and the inherent domain scale R. According to the common viewpoint, valid until recently, only for R matching λ a well-ordered morphology can be formed.[2,5,7,8,10,11,19,20] It was shown, however, that surface relief with $\lambda > R$ can align locally ordered grains of block copolymers into structures with a long-range order.[3,21] Also, our very recent results demonstrated that spin-coated ternary blend films form well-ordered lateral domains with the domain scale $R \sim \lambda/2$[22] (in accord with an earlier observation for ultrathin film of temperature quenched binary mixture).[12]

In the present work, the issue of $\lambda/2$-substructure formation in the spin-cast polymer blends is examined in the broader context of blend composition effects. The morphologies formed depend not only on spatial (R/λ) but also on compositional commensuration[17] between the binary blends and the symmetric pattern used, with one of two alternating surface stripes attracting selectively one (majority, minority, or symmetric) blend component: In addition to primary λ structures, $\lambda/2$-substructures are present when the selectively adsorbed polymer forms isolated (minority phase) but not continuous (majority phase) domains. For symmetric blends, pattern replication is affected by the transition from isolated to continuous domains, observed for (thicker) spin-cast films with larger R values. The impact of interfacial compatibilizer, present in ternary mixture, on pattern-ordered morphologies (with well-ordered substructures for both morphology types) is also analyzed.

Similarities and differences in the structures directed by the surface patterns (with two stripes: Au wetted by PVP[5,7,9,22] and neutral self-assembled monolayer[5,7,9,22−24]) are studied for spin-cast asymmetric (and off-critical, 2:3:0 and 3:2:0) and symmetric binary blends (1:1:0) and ternary mixtures (2:2:1) of the same model polymer system (poly(2-vinylpyridine) PVP/deuterated polystyrene PS/poly(methyl methacrylate) PMMA)[23,24] with different ratio of its components (PVP:PS:PMMA). To this end we have examined, by scanning probe microscopy (SPM), film topographies reflecting overall phase domain structures[5,7,9,22] formed on the same pattern for different casting conditions that varied the inherent structural scale R ($0.2\ \lambda \le R < 1.8\ \lambda$). The recorded morphologies were analyzed quantitatively with fast Fourier transform (FFT) analysis[7,11,12,22] and the recent extension[25,26] of the integral geometry approach.[27,28]

2. Experimental Section

Preparation of Polymer Films. Gold layers on Si wafers, covered or patterned with self-assambled monolayer (SAM) of hexadecanethiol [$HS(CH_2)_{15}CH_3$], formed homogeneous and patterned substrates used in this study. The former were

[†] Jagellonian University of Kraków, Poland.
[‡] AGH−University of Science and Technology, Kraków.
[§] NCRS "Demokritos", Greece.
* Corresponding author: e-mail ufbudkow@cyf-kr.edu.pl; Fax ++48-12-633 70 86; Ph 663 55 50.

10.1021/ma051242s CCC: $30.25
Published on Web 09/02/2005

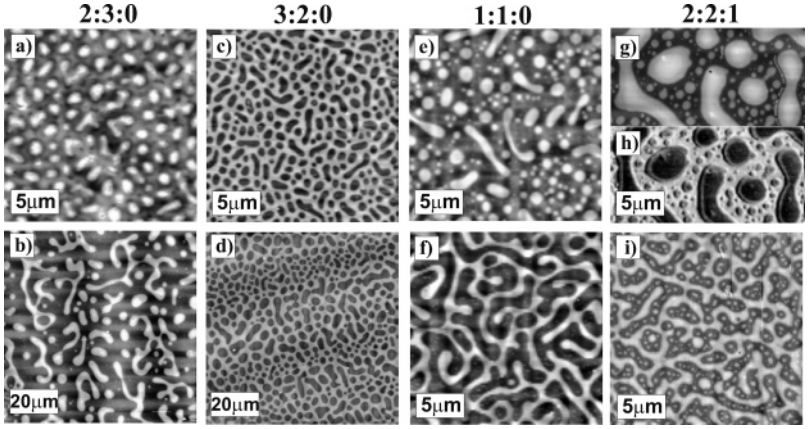

Figure 1. LFM (h) and AFM (a−g, i) images of PVP:PS:PMMA film blends 2:3:0 (a, b), 3:2:0 (c, d), 1:1:0 (e, f), and 2:2:1 (g−i) spin-cast onto homogeneous SAM substrate from THF solutions with constant spinning speed $\omega = 5800$ rpm and varied polymer concentration $c_P = 4.1$ (a, c), 5.4 (e), 6 (g, h), 7 (f), 9 (i), and 18 mg/mL (b, d). In (a−g, i) light areas are higher and dark are lower. In (h) white, gray, and black regions correspond to PS, PMMA, and PVP, respectively.

obtained when the wafers were immersed in ethanol solution of hexadecanethiol.[29] The latter, produced by microcontact printing method,[30] resulted in alternating symmetric stripes of pure Au and SAM (with width of ca. 2 μm and periodicity $\lambda = 4.0(1)$ μm).[7,22] The polymers used in the experiment were poly(2-vinylpyridine) (PVP, glass transition point $T_g = 357$ K,[31] molecular weigh $M_w = 115$K, polydispersity index $M_w/M_n = 1.02$), deuterated polystyrene (PS, $T_g = 373$ K,[31] $M_w = 174$K, $M_w/M_n = 1.03$), and poly(methyl methacrylate) (PMMA, $T_g = 379$ K,[31] $M_w = 149$K, $M_w/M_n = 1.1$), all purchased from Polymer Standards Service, Mainz, and used as obtained to prepare binary blends 2:3:0, 3:2:0, and 1:1:0 and ternary mixture 2:2:1 (mass fractions of PVP:PS:PMMA). For binary blends, the critical PVP weight fraction Φ_C is equal to 0.54. The polymers were dissolved in analytic grade tetrahydrofuran (THF), and the blend films were prepared by spin-coating with homemade coater or with a KW-4A apparatus, Chemat Technology, controlled by coating speed ω and total polymer concentration c_p ($\omega = 5800$ rpm and $2.6 \le c_p \le 18$ mg/mL for binary blends; $1700 \le \omega \le 5800$ rpm and $5.1 \le c_P \le 27$ mg/mL for 2:2:1). The average film thickness, determined from AFM images taken after partial film removal[24] from the control and selected experimental samples, ranged from 14 to 130 nm.

Surface Characterization. Topography and friction SPM images of the cast thin films were collected in air at room temperature by atomic (AFM) and lateral (LFM) force modes of CP Park Scientific Instruments microscope (scan range up to 80 μm × 80 μm) working in contact mode with a Si_3N_4 tip and a typical load of 4 nN. LFM resolves domains rich in PVP, PS, and PMMA.[24,32] The SPM data illustrate overall phase domain structure, as confirmed for this system[7,9,20,22,24,32] by a composition mapping mode of dynamic secondary ion mass spectrometry (dSIMS)[7,9,22] and by AFM combined with selective dissolution of PVP and PS.[7,9,20,24,32] In the former method, a few composition maps of PVP (CN^- ions, $m/z = 26$, typically with Rayleigh lateral resolution of ~120 nm) were collected for successive depth values in the analyzed sample. The dSIMS apparatus (produced by Vacuum Science Workshop) was equipped with high-resolution ion gun (double lens, liquid metal source, produced by Fei Co.) and quadrupole mass spectrometer (Balzers) with a cylindrical mirror energy filter at the entrance.[33] All structures shown in the AFM/LFM images were reproducible, independent of scan direction or scan range. Images with different range were collected to provide data optimal for image analysis. The blend films formed on homogeneous and patterned substrates in the same spin-casting conditions (ω, c_p) were recorded by SPM as pairs of isotropic and anisotropic morphologies.

Image Analysis. The topographic (AFM) images were examined numerically with Fourier analysis[7,22] and the integral geometry approach[25] using the software developed in our laboratory.[7,22,25] For each AFM image its 2-dimensional fast Fourier transform (FFT) was computed.[7,22] The FFT spectrum of isotropic morphology is characterized by an isotropic diffuse ring with $|\mathbf{k}| = k^*$. The radial average $P_i(k)$ of the squared FFT amplitudes was used to determine (Lorentz line fit) the radius k^* of the ring at its maximum and the inherent domain scale $R = 1/k^*$. The FFT image of anisotropic topography exhibits two components: the ring and a slanting line of diffraction peaks with $\mathbf{k} = n\mathbf{k}_\lambda$ (n is an integer, $|\mathbf{k}_\lambda| = 1/\lambda$). The squared FFT amplitudes of the $\mathbf{k}$-region forming a narrow (4 pixels wide) stripe along the $n\mathbf{k}_\lambda$ peaks were averaged to yield the total power spectrum $P(k)$. The isotropic contribution $P_i(k)$, defined by the radial averaged data of the $\mathbf{k}$-plane without $n\mathbf{k}_\lambda$ stripe, was removed from $P(k)$ to yield the spectrum $P_a(k)$ of the anisotropic component, discussed in detail later. The ratio $\tilde{P}_a/\tilde{P}$ of the integrated power spectra $P_a(k)$ and $P(k)$ was used as a measure of morphological anisotropy. For each AFM image of the surface (with bimodal height h-distribution centered at $\langle h_1 \rangle$ and $\langle h_2 \rangle$), the Euler characteristic χ_E (connectivity) of elevated regions (i.e., with local height $h > (\langle h_1 \rangle + \langle h_2 \rangle)/2$) was calculated.[25] χ_E is defined as the difference between the number of separated elevated and depressed regions normalized by the analyzed area. For hierarchical morphologies the χ_E values are computed for all and for dominant (i.e., with the structures smaller than 15% of R neglected) surface features.

3. Results and Discussion

3.1. Blends on Homogeneous SAM. Quasi-2D Domain Structure. We start our discussion with phase demixing in polymer film blends and focus later (next paragraph) into adsorption-driven pattern-guided alignment of the demixed phases. The former process occurs for the studied PVP:PS:PMMA blends[5,7,9,20,22−24,32] spin-cast from a common solvent (THF) onto homogeneous SAM substrate (Figure 1): None of the three polymers (PVP, PMMA, PS) wets either the free surface or the substrate[5,7,9,20,22−24,32] of the formed films (cast either from high, THF, or low volatile solvent[20,32]). These films (with morphologies practically identical[23,32] to those obtained in 2D simulations of solvent-free mixture[34]) are reported[5,7,9,20,22−24,32] to be quasi-2-dimensional systems with lateral phase structure extending from surface throughout the film to the substrate (realized in films with symmetric neutral surfaces[35]). At late stages of spin-casting, PVP and PMMA, which are both less soluble in a common solvent (THF),[5,23,36] solidify due to solvent evaporation earlier than PS,[23,36] leading to the collapse of the initially THF-swollen PS-rich areas below the level of PVP- and PMMA-rich phase. Thus, in the final solvent-free film (Figure 1), PVP and PMMA domains are elevated while PS-rich regions depressed,

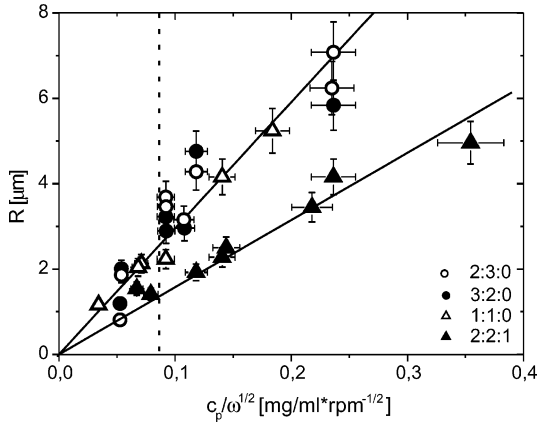

Figure 2. Inherent scale of lateral domains R formed by PVP:PS:PMMA film blends 2:3:0 (open circles), 3:2:0 (solid circles), 1:1:0 (open triangles), and 2:2:1 (solid triangles) on homogeneous SAM substrate as a function of $c_P/\omega^{1/2}$. Solid lines represent linear relations determined for binary and ternary blends. The dashed line marks the spin-casting conditions ($c_P/\omega^{1/2}$ value) corresponding to the transition from isolated to continuous PVP domains (observed for 1:1:0 and 2:2:1).

and the phase morphology is mirrored by the film topography.[5,7,9,20,22−24,32] Therefore, the phase distribution of these quasi-2D systems is revealed by topography analysis,[5,7,9,20,22−24,32] consistent with the results of complementary methods such as LFM,[22,24,32] mapping dSIMS,[7,9,22] and AFM combined with selective dissolution.[5,7,9,20,23,24,32]

Tunable Structural Scale *R*. During spin-casting the polymers dissolved in THF form initially a homogeneous liquid film. Liquid flow, which is caused by a balance between centrifugal and viscous forces, decreases film thickness and controls its final value $h \sim c_P/\omega^{1/2}$ [37−39] (demonstrated for PVP:PS:PMMA[22,24]), adjusted by spinning speed ω and polymer concentration c_P in the solvent. Phase separation, initiated by evaporating THF, takes place simultaneously with film thinning and is terminated when solvent concentration is so low that polymer molecules are no longer mobile. For thicker films solvent drying and phase coarsening takes place during a longer period of time leading to lateral morphologies with a larger domain scale R (cf. Figure 1a,b or Figure 1c,d). A linear scaling relation $R \sim h$ between horizontal and vertical scales of the film structure was concluded for the binary[40] and ternary[24] blends PVP:PS:PMMA. To show how the inherent domain scale R of both film blend types depends on the spin-casting conditions (ω,c_P), we have plotted R as a function of $c_P/\omega^{1/2}$ (Figure 2). Four data sets correspond to R values determined with FFT analysis for 2:3:0 (open circles), 3:2:0 (solid circles), 1:1:0 (open triangles), and 2:2:1 films (solid triangles). All three binary blend data sets are scattered (due to limited reproducibility in ω and c_P) along the same linear relation marked by solid line and described by linear coefficient 29.3 ± 1.0 μm mL rpm$^{1/2}$/mg. This might suggest (i) similar solvent-quench paths and drying times when casting conditions are fixed and (ii) final phase evolution regime of the same spinodal-decomposition type for continuous and droplet morphologies.[41] In turn, the ternary mixture data set is described by the linear relation (second solid line in Figure 2) with much lower coefficient of 15.7 ± 0.7 μm mL rpm$^{1/2}$/mg. For constant casting conditions the domain scale R is reduced considerably for the 2:2:1 films. To obtain for both blend types the morphologies with comparable lateral scale, the spinning speed ω must be reduced or polymer concentration c_P increased for 2:2:1 as compared with binary mixtures (cf. Figure 1i,f). The results presented in Figure 2 demonstrate quantitatively that PMMA enhances compatibility of the PVP:PS system.[23] The interfacial energy is the driving force in various phase coarsening regimes[9,42] along the solvent-quench path, and its reduction leads to slower kinetics and hence to smaller morphological scale R for fixed casting conditions (or longer coarsening time for constant R). To reduce the interfacial energy, and as a consequence of mutual incompatibility (expressed by interaction parameters: $\chi_{PS/PVP} = 0.1 \gg \chi_{PS/PMMA} \approx 0.02$, $\chi_{PVP/PMMA} \approx 0.007$),[23] PMMA intercalates at the PS:PVP interfaces[23,24] and separates PS- and PVP-rich phases (Figure 1h).

Isolated and Continuous Domains. While the phase separation process that takes place during spin-casting[37−39,43] is not completely resolved, different phase evolution patterns[32] (or their combinations)[26,29,32] have been recognized: In addition to bulk coarsening confined by film geometry into two dimensions[23−25,44] (with secondary phase separation allowed),[24,45] the final phase arrangement can be affected by the (capillary, dewetting) instability of phase-phase interface (breaking up transient multilayer phase arrangement)[26,32,44,46,47] and by the (hydrodynamic, convective) instability[29,32,48,49] of the free film surface. These commonly accepted features allow us to explain the observed film morphologies (Figure 1). When a longer film formation time is allowed (with $c_P/\omega^{1/2} \geq 0.09$ mg/(mL rpm$^{1/2}$)) the compositional dependence of film topography (Figure 1b,d,f,i) suggests that morphology formation mechanism is dominated by bulk coarsening confined to two dimensions:[23−25,44,50−52] Two droplet-type morphologies, dominated by PVP-rich islands (blend 2:3:0, Figure 1b) or PS-rich holes (blend 3:2:0, Figure 1d), are separated by bicontinuous structures at intermediate composition (blend 1:1:0, Figure 1f)—matching the critical value $\Phi_C = 0.54$. In turn, hierarchical morphologies with two length scales (dominant and secondary) are present in the blend films 2:2:1 (Figure 1g−i): Here the secondary structures of small circular inclusions in the PS-rich depletions are attributed[22,24] to the secondary phase separation process[45] effective in the fast formed PS-rich domains (with transient composition far from equilibrium values), where the solvent is depleted later and polymers are mobile longer.

For thicker films quasi-2D phase coarsening takes place during a longer period of time. As a result, self-similar growing structures are observed[7,24,44] for increasing $c_P/\omega^{1/2}$: They are formed always for asymmetric blends (2:3:0 and 3:2:0) with droplet-type morphologies (Figures 1a,b and 1c,d), but in the 2:3:0 layers the self-similarity of the morphology shown in Figure 1a is somewhat affected for the longest film formation time (Figure 1b) when first effects of free surface instability[32] modify PVP domain coalescence on a scale larger than the domains. In turn, for both mixtures 1:1:0 and 2:2:1 self-similar morphologies with bicontinuous dominant structures (resembling these of Figure 1f,i) are formed only for $c_P/\omega^{1/2} \geq 0.09$ mg/(mL rpm$^{1/2}$). Distinct dominant structures with isolated domains are observed when the films are formed more rapidly (Figure 1e,g,h). This morphological transition is marked as the dashed line in Figure 2. The circular droplets visible in Figure 1e,g,h suggest the effects of interfacial (capillary) instabil-

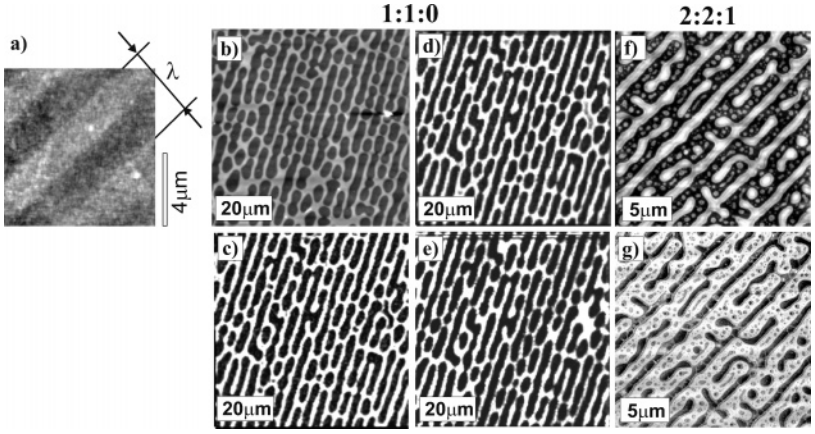

Figure 3. LFM (a, g), AFM (b, f), and dSIMS (c−e) images illustrating the transposition of the substrate pattern Au/SAM (a) into the films 1:1:0 (b−e) (c_P = 14 mg/mL, ω = 5800 rpm) and 2:2:1 (f−g) (c_P = 9 mg/mL, ω = 5800 rpm). Film topography (b, f) reflects domain structure determined (another spots) at the distance z = 0 (g), 18 (c), 55 (d), and 92 nm (e) from air surface. Light regions in (a) and (c−e) correspond to original Au stripes (covered with $HS(CH_2)_{15}COOH$ to improve contrast) and PVP domains, respectively. White, gray, and black regions in (g) correspond to PS, PMMA, and PVP, respectively.

ity[26,47] breaking up transient multilayer solvent-rich phase arrangement (e.g., created due to different polymer solidification rate).[46,47] Such a formation scenario[26,47] can be supplemented[26] by quasi-2-dimensional phase coarsening, resulting in more elongated domains present in addition to circular droplets. In turn, the effects of free surface (convective) instability are here not observed for the range of spin-casting conditions used.[40]

3.2. Mixtures on Au/SAM Pattern. The organization of lateral domains of PVP:PS:PMMA blends (Figure 3b−g) on the substrate with Au/SAM pattern (Figure 3a) is driven by strong affinity of PVP to the Au surface regions[5,7,9,20,22] demonstrated earlier with different techniques (depth profiling and imaging dSIMS,[7,9,22] AFM combined with selective dissolution[5,7,9,20]). A PVP-rich phase (white and black regions in parts b−f and g of Figure 3, respectively) forms on the Au stripes PVP domains of the primary λ-structure but can extend elsewhere and/or direct PVP domains of the substructure (e.g., Figure 3f,g). The compliance of film morphology with the periodic substrate pattern is described below for four different mixtures (2:3:0, 3:2:0, 1:1:0, 2:2:1). Its analysis is based on four topographic sequences (exemplified by parts a−e, f−j, k−o, and p−u of Figure 4, respectively) of spin-cast films "frozen" for increasing both the drying time (i.e., thickness $h \sim c_P/\omega^{1/2}$) and inherent scale R of coarsening lateral domains ($0.2 \leq R/\lambda < 1.8$). Each sequence resembles structures evolving during quasi-2-dimensional phase coarsening;[53] however, the effects of interfacial and surface instabilities are also relevant.[54]

Blends 2:3:0. The first AFM image of this series (Figure 4a) illustrates practically isotropic domains of the size $R/2 \sim 0.4$ μm with some weak traces of linear domain arrays. The next figure (Figure 4b), corresponding to $R \sim 0.47$ λ, shows elongated PVP droplets in register with an underlying pattern with periodicity λ and located between them slightly smaller droplets of a weak $\lambda/2$-substructure. The coalescence[41] of PVP droplets is more effective along the Au stripes, resulting in the primary λ-structure. Other PVP droplets appear with interdomain spacing $R \sim \lambda/2$ away from the primary structure, forming the substructure. This $\lambda/2$-ordering effect is enhanced by the strips depleted in PVP, adjacent to the primary structure and separating it from the substructure. For longer drying times (Figure 4c,d) the coalescing PVP droplets forming the primary structure become much more distinct than droplets formed on neutral SAM stripes. In turn, Figure 4e corresponding to $R \sim 1.8\lambda$ and the longest film formation time shows large elongated PVP domains (due to initial effects of free surface instability), comparable in size to those observed on the homogeneous SAM substrate (Figure 1b) but with the domains aligned along the Au stripes.

Blends 3:2:0. This sequence starts, for $R \sim 0.3\lambda$ (Figure 4f), with almost isotropic morphology dominated by polydispersive (in size) PS-rich holes (cf. Figure 1c) surrounded by continuous elevated PVP-rich ribbons, which show weak sporadic alignment along parallel lines. The next AFM image (Figure 4g), corresponding to $R \sim \lambda/2$, shows the Au stripes coated in their centers by PVP ribbons intruding elsewhere to enclose larger PS droplets and covered to their complete lateral extension by small PS domains encircled by PVP-rich elevations. Superfluous PVP material (major blend component) forms numerous bridges between the elevations lined in register with the Au stripes. No $\lambda/2$-substructures are formed midway between them. The alignment of such linear elevations is improved for larger R values (Figure 4h,i). Simultaneously, the number of the bridges is reduced (Figure 4h) to reach the minimum for the domain scale R almost matching the pattern periodicity λ (Figure 4i). When the inherent scale R of domain structure is larger than pattern periodicity λ (Figure 4j), the bridges, linking the PVP elevations above the Au stripes, are formed again, and the periodic elevations become less ordered. For the 3:2:0 films quasi-2D phase coarsening is enhanced on the pattern (e.g., compare hole density in films cast at the same conditions: Figure 1c and the framed region of Figure 4g or in Figure 1d and Figure 4j). The relevant mechanism includes the transport of PVP material to the linear regions wetting Au stripes through continuous PVP-rich tubes, driven by the curvature of phase boundaries between PVP-rich and PS-rich phases (analogously to hydrodynamic flow-driven wetting of blend surfaces).[55−57]

Blends 1:1:0. The first image of this series (Figure 4k) illustrates a completely isotropic structure composed of isolated circular droplets, only sporadically coalesced into elongated domains. Both missing reaction to the substrate pattern and the domain size $R/2 \sim 0.6$ μm

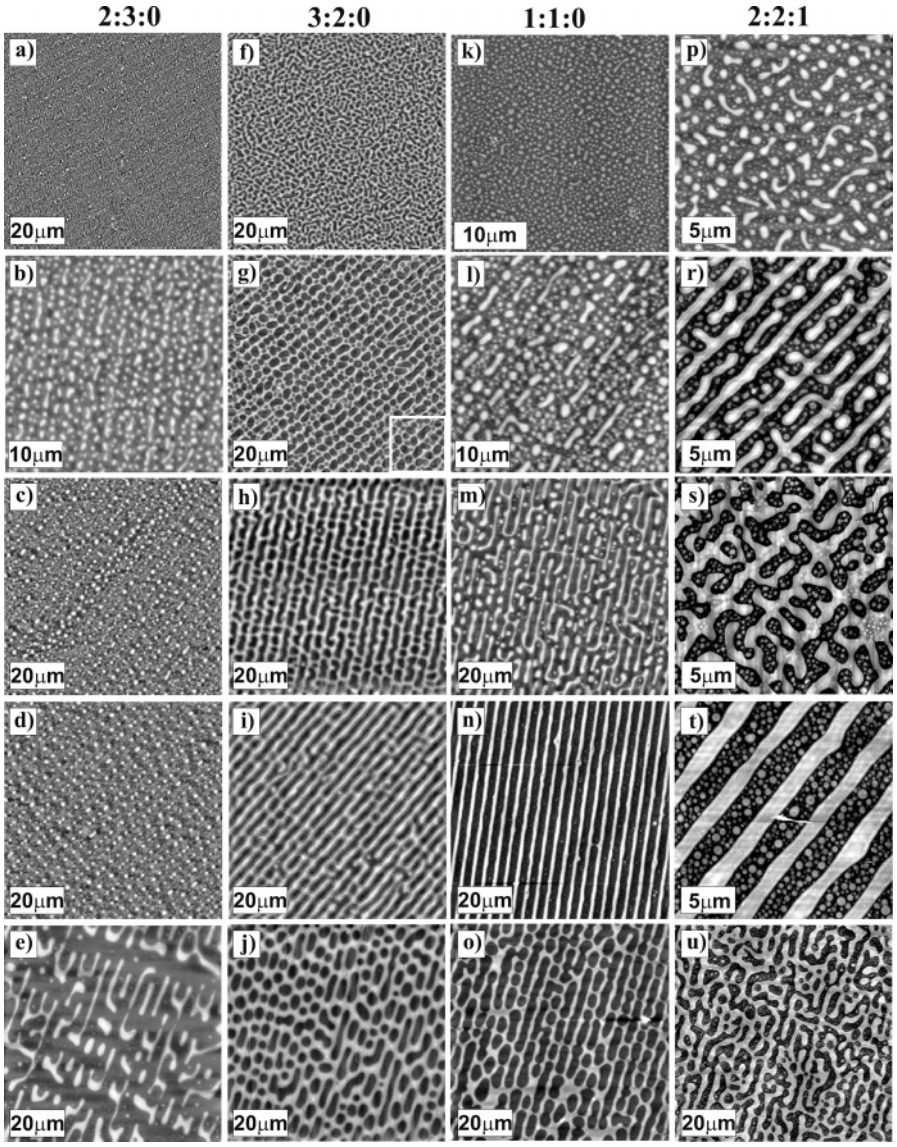

Figure 4. AFM images of film blends 2:3:0 (a−e), 3:2:0 (f−j), 1:1:0 (k−o), and 2:2:1 (p−u) cast ($\omega = 5800$ rpm) from THF solutions with different polymer concentration $2.6 \leq c_P \leq 27$ mg/mL to form morphologies with controlled inherent domain scale $R < \lambda/2$ (a, f, k, p), $R \sim \lambda/2$ (b, g, l, r), $R > \lambda/2$ (c, h ,m, s), $R \sim \lambda$ (d, i, n, t), and $R > \lambda$ (e, j, o, u).

much larger than the dominant heterogeneity length[58] ($\Lambda_m \sim 0.01$ μm, characteristic for the early stage of spinodal decomposition in the melt) indicate that quasi-2-dimensional coarsening is not very effective here and support the scenario of interfacial instability. The subsequent figure (Figure 4l), corresponding to $R \sim \lambda/2$, shows the elongated PVP domains of the primary λ-structure (in register with the periodic pattern of Au stripes) and, located between them, smaller droplets contributing to the $\lambda/2$-substructure ($\lambda/2$-ordering effect, cf. Figure 4b for 2:3:0). Quasi-2D phase coarsening, which supplements structure formation due to interfacial instability,[59] results in the progressive (with R) coalescence of PVP droplets most effective along the Au stripes. The next AFM image (Figure 4m), although with similar value of $R \sim 0.56\lambda$, shows different morphology: Large elongated PVP domains, in register with the substrate pattern, are often interconnected while the small droplets of the $\lambda/2$-substructure are much less frequent than previously. This morphological change corresponds to that observed for the homogeneous substrate (Figure 1e,f), where the (self-similar) bicontinuous (dominant) structures appear for $c_P/\omega^{1/2} \geq 0.09$ mg/(mL rpm$^{1/2}$) (dashed line in Figure 2), reflecting the decisive role of quasi-2D coarsening. The $\lambda/2$-substructure disappears completely for larger R values. Simultaneously, the continuity of the primary PVP-rich elevations is improved while the number of bridges linking them is reduced for the domain scale R matching the pattern periodicity λ (Figure 4n, cf. Figure 4i for 3:2:0). When the scale R is larger than λ (Figure 4o), then the bridges are formed again while the periodic elevations remain continuous along the Au stripes.

Blends 2:2:1. All AFM pictures (Figure 4p−u) show here hierarchical morphologies with the secondary structures (due to secondary phase separation) practically irrelevant for pattern transposition in contrast to the dominant surface features discussed below. While the sequences for binary mixtures of comparable structural scale R begin with almost isotropic morphologies (Figure 4a,f,k), this series starts with strongly anisotropic structure ($R \sim 0.3\lambda$, Figure 4p): The more elongated PVP-rich droplets are located on the periodic Au stripes and order the less extended domains to form the $\lambda/2$-substructure ($\lambda/2$-ordering effect, cf. Figure 4b,l). Both the primary λ-structure and the $\lambda/2$-substructure,

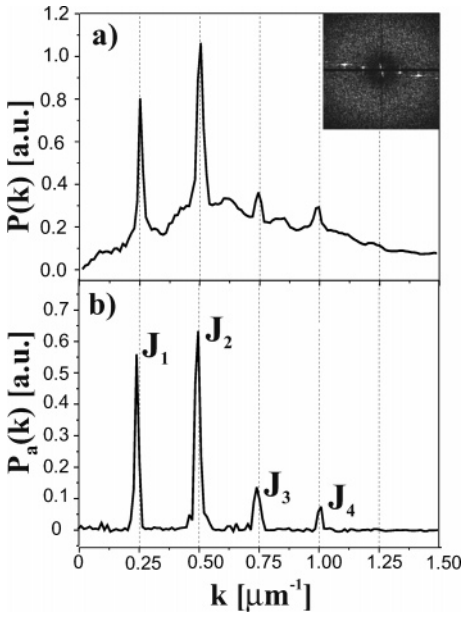

Figure 5. Total power spectrum $P(k)$ (a) and the spectrum $P_a(k)$ of anisotropic component (b), computed (along the peaks $n\mathbf{k}_\lambda$) for 2D FFT image (see the inset corresponding to Figure 4b). J_n ($n = 1, 2, 3, 4$) denotes the intensity of peaks positioned at $n\mathbf{k}_\lambda$ ($|\mathbf{k}_\lambda| = 1/\lambda$).

originating from interfacial instability, are well developed as a result of quasi-2D phase coarsening. The role of the latter increases for the ternary 2:2:1 blend as compared with binary mixtures since longer structure formation times (larger $c_P/\omega^{1/2}$ values in Figure 2) are available to form morphologies with comparable R value. Additionally, the transition into continuous (dominant) film structures [observed at $c_P/\omega^{1/2} \sim 0.09$ mg/(mL rpm$^{1/2}$)] occurs here for smaller R values ($R/\lambda \sim 0.43$, Figure 4p,r) than in the films 1:1:0 ($R/\lambda \sim 0.55$, Figure 4l,m). Well-ordered elongated domains with the $\lambda/2$-periodicity (Figure 4r) are formed already after the transition. Low energetic interfaces form extensive substructures connected with the continuous linear elevations of the λ-structure. Such primary elevations are linked by the bridges (Figure 4s), created by the substructure domains extending into both neighboring elevations when the interdomain spacing R is larger than $\lambda/2$. This picture is drastically modified (Figure 4t) for the domain scale R matching the period λ of the substrate pattern, perfectly reproduced by the linear elevations of the primary λ-structure (cf. Figure 4i,n). For R larger than λ the bridges are formed again by apparently too large domains of the λ-structure (Figure 4u).

Fourier and Integral Geometry Analysis. The Fourier analysis[7,22] is based on the 2D FFT image (e.g., see the inset in Figure 5) of AFM picture (here Figure 4b): The power spectrum $P(k)$ (Figure 5a) computed along the slanting line of diffraction peaks $\mathbf{k} = n\mathbf{k}_\lambda$ (n is an integer) includes the isotropic contribution (parts of diffusive ring), which is removed (see Experimental Section) to yield the spectrum $P_a(k)$ of anisotropic component (Figure 5b). The ratio $\tilde{P}_a/\tilde{P}$ of the integrated spectra $P_a(k)$ and $P(k)$ measures the morphological anisotropy. The spectrum $P_a(k)$ (Figure 5b) exhibits several peaks positioned at $n\mathbf{k}_\lambda$ ($|\mathbf{k}_\lambda| = 1/\lambda$) and characterized by absolute $J_n = J(n\boldsymbol{k}_\lambda)$ and relative intensities $I_n = J_n/\sum_m J_m$. These intensities are used to measure the order of lateral domains forming the primary λ-structure (I_1) and the $\lambda/2$-substructure (I_2). Such an analysis, performed for the topographic data, is representative for the entire film morphology, the surface topography as well as the domain structure. Such conclusions come out from the comparison[7,22] of the intensities I_n obtained for (AFM) topographic and (dSIMS) PVP distribution maps recorded for binary[7] and ternary[22] PVP:PS:PMMA films.

For all film blends the results of the Fourier analysis (the ratio $\tilde{P}_a/\tilde{P}$ and the relative intensities I_n) are plotted in Figure 6 vs the degree of commensurability R/λ. The films 2:3:0 with isolated PVP domains exhibit strong anisotropy (large and nearly constant $\tilde{P}_a/\tilde{P}$ values, Figure 6a) and weak $\lambda/2$-substructures with long-ranged order confirmed by the Fourier peak intensities: I_2 is weakly larger than I_1 for $R \sim \lambda/2$ and only slightly lower than I_1 for $R \sim \lambda$ (Figure 6b). In turn, the films 3:2:0 with continuous PVP phase show no traces of the substructure ordering ($I_2 \ll I_1$ for both $R \sim \lambda/2$ and $R \sim \lambda$, Figure 6d) and morphological anisotropy (Figure 6c) peaked at commensurate R and λ, reflecting enhanced domains compliance to the pattern. The situation in the films 1:1:0 (Figure 6e,f) can be explained by the morphological transition (at $R/\lambda \sim 0.55$) from isolated (as in 2:3:0) to continuous PVP domains (as in 3:2:0). Ordered $\lambda/2$-substructures [with maximal $I_2 = 0.57(6)$ weakly larger than corresponding $I_1 = 0.43(4)$] are destroyed ($I_2 \ll I_1$), and the primary structures comply strongly with the pattern (maximal $\tilde{P}_a/\tilde{P}$ value at $R \sim \lambda$). In turn, for the ternary mixtures 2:2:1 (Figure 6g,h) the well-ordered $\lambda/2$-substructures are present for both isolated [$I_2 = 0.61(6)$, $I_1 = 0.24(2)$, for $R/\lambda = 0.38$] and continuous PVP domains [$I_2 = 0.67(7)$ and $I_1 = 0.11(1)$ at $R = 0.48\ \lambda$] around the transition. For larger domain scales, the dominant primary structures with the highest $\tilde{P}_a/\tilde{P}$ values are observed in the region $R \sim \lambda$.

The Euler characteristic χ_E of the film topographies, yielded by the integral geometry approach,[25] is presented in Figure 7 as a function of the domain scale R. The morphological measure χ_E reflects difference between surface density of distinct elevated and depressed regions. Positive χ_E values, determined for the films 2:3:0 with (PVP-rich) islands (Figure 7a), are scattered along the scaling relation (solid line) $\chi_E \sim 1/R^2$,[25,27] but do not reflect any reaction of domain ordering for the domain scale R comparable to the pattern period λ. In contrast, the negative measure χ_E, reflecting 3:2:0 film morphologies dominated by (PS-rich) holes, shows the minimum $|\chi_E| \to 0$ for $R \sim \lambda$ (Figure 7b). The zero value of the Euler characteristic χ_E, reflecting perfect pattern transposition for commensurate R and λ, appears again for all (open diamonds) and dominant surface features (with small-scale corrugations neglected, solid squares) of the films 1:1:0 ($R \sim \lambda$, Figure 7c) and 2:2:0 ($R \sim \lambda/2$ and $R \sim \lambda$, Figure 7d), respectively.

4. Summary and Conclusions

We describe the transposition of the symmetric substrate pattern, composed of alternating (with a micrometer period λ) stripes of neutral (SAM) and selectively adsorbing regions (Au wetted by PVP), into the lateral morphology of spin-cast (with varied structural scale R) blends PVP:PS:PMMA (2:3:0, 3:2:0, 1:1:0, 2:2:1). Pattern transposition depends not only on spatial (R/λ) but also compositional commensuration[17] between blend and symmetric pattern: $\lambda/2$-substructures are present, in

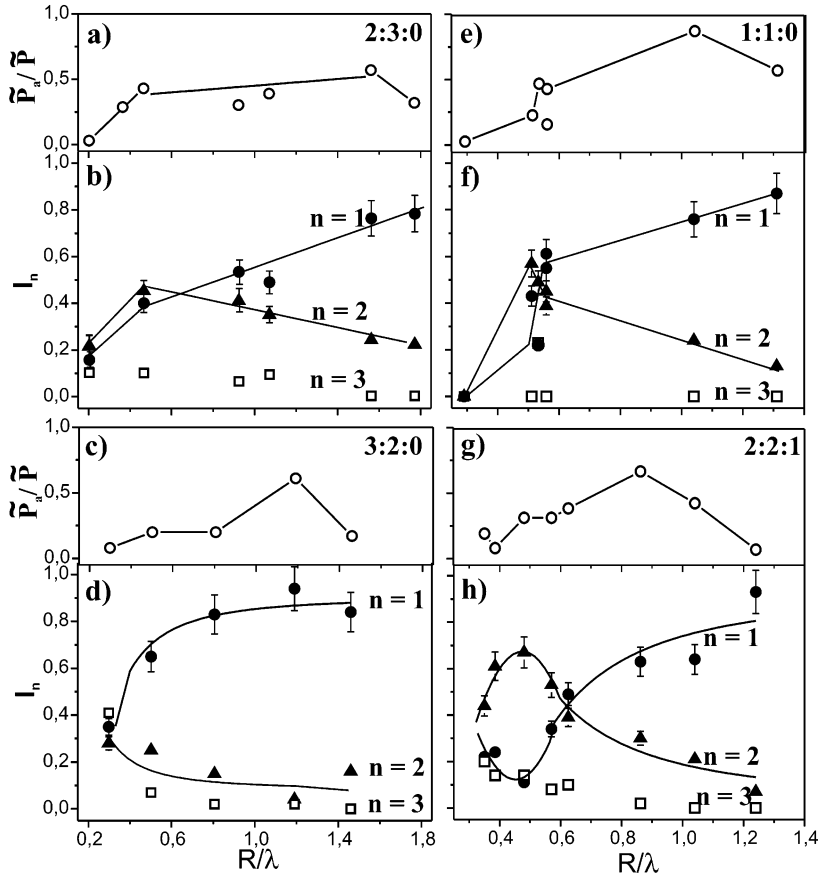

Figure 6. Results of FFT analysis of film blends 2:3:0 (a, b), 3:2:0 (c, d), 1:1:0 (e, f), and 2:2:1 (g, h) cast on the pattern, plotted vs the degree of commensurability R/λ. (a, c, e, g) The ratio $\tilde{P}_a/\tilde{P}$ of the integrated power spectra $P_a(k)$ and $P(k)$. (b, d, f, h) Relative intensities $I_n = J_n/\sum_m J_m$ ($n = 1, 2, 3$).

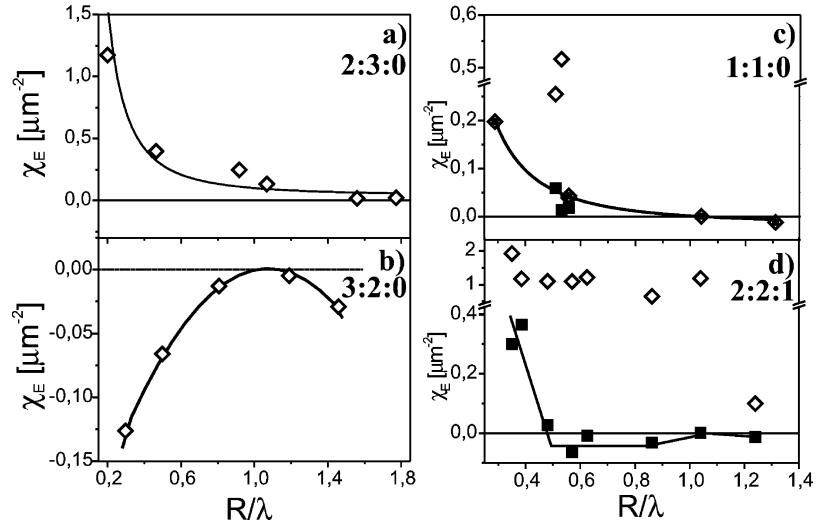

Figure 7. Euler characteristic χ_E of the surface morphologies formed by the films 2:3:0 (a), 3:2:0 (b), 1:1:0 (c), and 2:2:1 (d), plotted vs the degree of commensurability R/λ. The data points marked by open diamonds and solid squares correspond to all and to dominant surface features, respectively.

addition to λ-structures, for isolated (2:3:0) but not for continuous (3:2:0) PVP domains (Figure 6b,d), which constitute minor and major blend component, respectively. In films 2:3:0 droplet growth,[41] pattern-guided by selective adsorption, results in primary structures formed at the expense of adjacent zones depleted in PVP, which order the substructure domains (Figure 4b). In turn, enhanced phase coarsening observed in films 3:2:0 (with no substructures) is plausibly related with the hydrodynamic flow-driven wetting[55−57] of the selective Au stripes involving PVP transport through continuous tubes of its majority phase (Figure 4g,h). These different quasi-2D coarsening scenarios for isolated and continuous PVP domains can explain pattern transposition in the films 1:1:0 (Figure 6f), where isolated droplets (Figure 4l) transform into continuous domains (Figure 4m) for larger R values. When the films are formed very rapidly, quasi-2D coarsening is initiated but does not become dominant, and therefore isolated droplets are present, originating from interfacial insta-

bility.[32,59] In turn, surface instability is not effective here[40] (only some initial traces are visible in 2:3:0, Figure 4e). The transition from droplet to continuous (dominant) morphology is observed also in the films 2:2:1, but the well-ordered $\lambda/2$-substructures (Figure 6h) are formed for both morphology types (Figure 4p,r). Interfacial active PMMA results in low-energetic lateral interfaces which form well-developed substructures (because, for comparable R, film formation in 2:2:1 is longer, Figure 2). Such interfaces are more extended and ordered for continuous PVP domains (in contrast to binary blends). Continuous morphology of PVP-rich phase enhances collective compliance to the substrate pattern (Figures 6c,e,g and 7b−d) when the scale R is commensurate with pattern periodicity λ ($R/\lambda \sim 0.5$ for blends 2:2:1 and $R/\lambda \sim 1$ for mixtures 2:2:1, 1:1:0, 3:2:0). Well-ordered elongated domains with the $\lambda/2$-periodicity formed in films 2:2:1 are related with blend compatibility enhanced by PMMA whereas volume fraction effects are excluded based on the comparison with the mixtures 2:3:0 and 3:2:0.

Acknowledgment. This work was partially supported by the Reserve of the Rector of the Jagellonian University and the Polish Committee for Scientific Research (mainly by Grant 1P03B01027). We thank Dr. R. Dahint (Heidelberg) for PDMS stamps and Prof. M. Szymoński for the access to the AFM apparatus. We acknowledge with thanks Prof. U. Steiner for his contribution to the early stage of this project.

References and Notes

(1) Hamley, I. W. *Angew. Chem., Int. Ed.* **2003**, *42*, 1692. Park, C.; Yoon, J.; Thomas, E. L. *Polymer* **2003**, *44*, 6725.
(2) Rockford, L.; Liu, Y.; Mansky, P.; Russell, T. P.; Yoon, M.; Mochrie, S. G. J. *Phys. Rev. Lett.* **1999**, *82*, 2602.
(3) Segalman, R. A.; Yokoyama, H.; Kramer, E. J. *Adv. Mater.* **2001**, *13*, 1152.
(4) Krausch, G.; Kramer, E. J.; Rafailovich, M. H.; Sokolov, J. *Appl. Phys. Lett.* **1994**, *64*, 2655.
(5) Böltau, M.; Walheim, S.; Mlynek, J.; Krausch, G.; Steiner, U. *Nature (London)* **1998**, *391*, 877.
(6) Fukunaga, K.; Elbs, H.; Krausch, G. *Langmuir* **2000**, *16*, 3474.
(7) Cyganik, P.; Bernasik, A.; Budkowski, A.; Bergues, B.; Kowalski, K.; Rysz, J.; Lekki, J.; Lekka, M.; Postawa, Z. *Vacuum* **2001**, *63*, 307.
(8) Li, X.; Xing, R.; Zhang, Y.; Han, Y.; An, L. *Polymer* **2004**, *45*, 1637.
(9) Budkowski, A.; Bernasik, A.; Cyganik, P.; Rysz, J.; Brenn, R. *e-Polym.* **2002**, 006.
(10) Karim, A.; Douglas, J. F.; Lee, B. P.; Glotzer, S. C.; Rogers, J. A.; Jackman, R. J.; Amis, E. J.; Whitesides, G. M. *Phys. Rev. E* **1998**, *57*, R6273.
(11) Ermi, B. D.; Nisato, G.; Douglas, J. F.; Rogers, J. A.; Karim, A. *Phys. Rev. Lett.* **1998**, *81*, 3900.
(12) Nisato, G.; Ermi, B. D.; Douglas, J. F.; Karim, A. *Macromolecules* **1999**, *32*, 2356 (see Figure 14).
(13) Yoo, P. J.; Suh, K. Y.; Lee, H. H. *Macromolecules* **2002**, *35*, 3205.
(14) Park, C.; Yoon, J.; Thomas, E. L. *Polymer* **2003**, *44*, 6725.
(15) Shimoda, T.; Morii, K.; Seki, S.; Kiguchi, H. *MRS Bull.* **2003**, November, 821.
(16) Wang, Q.; Nath, S. K.; Graham, M. D.; Nealey, P. F. *J. Chem. Phys.* **2000**, *112*, 9996.
(17) Kielhorn, L.; Muthukumar, M. *J. Chem. Phys.* **1999**, *111*, 2259.
(18) Shou, Z.; Chakrabarti, A. *Polymer* **2001**, *42*, 6141.
(19) Fasolka, M. J.; Harris, D. J.; Mayes, A. M.; Yoon, M.; Mochrie, S. G. J. *Phys. Rev. Lett.* **1997**, *79*, 3018.
(20) Sprenger, M.; Walheim, S.; Schäffer, C.; Steiner, U. *Adv. Mater.* **2003**, *15*, 703.
(21) Cheng, J. Y.; Ross, C. A.; Thomas, E. L.; Smith, H. I.; Vansco, G. J. *Appl. Phys. Lett.* **2002**, *81*, 3657.
(22) Cyganik, P.; Budkowski, A.; Steiner, U.; Rysz, J.; Bernasik, A.; Walheim, S.; Postawa, Z.; Raczkowska, J. *Europhys. Lett.* **2003**, *62*, 855.
(23) Walheim, S.; Ramstein, M.; Steiner, U. *Langmuir* **1999**, *15*, 4828.
(24) Cyganik, P.; Budkowski, A.; Raczkowska, J.; Postawa, Z. *Surf. Sci.* **2002**, *507−510*, 700.
(25) Raczkowska, J.; Rysz, J.; Budkowski, A.; Lekki, J.; Lekka, M.; Bernasik, A.; Kowalski, K.; Czuba, P. *Macromolecules* **2003**, *36*, 2419.
(26) Raczkowska, J.; Bernasik, A.; Budkowski, A.; Sajewicz, K.; Penc, B.; Lekki, J.; Lekka, M.; Rysz, J.; Kowalski, K.; Czuba, P. *Macromolecules* **2004**, *37*, 7308.
(27) Mecke, K. R. *Phys. Rev. E* **1996**, *53*, 4794−4800; *Int. J. Mod. Phys. B* **1998**, *9*, 861.
(28) Michielsen, K.; De Raedt, H. *Phys. Rep.* **2001**, *347*, 461.
(29) Budkowski, A.; Bernasik, A.; Cyganik, P.; Raczkowska, J.; Penc, B.; Bergues, B.; Kowalski, K.; Rysz, J.; Janik, J. *Macromolecules* **2003**, *36*, 4060.
(30) Xia, Y.; Whitesides, G. M. *Angew. Chem., Int. Ed.* **1998**, *37*, 550.
(31) Mark, J. E. *Polymer Data Handbook*; Oxford University Press: New York, 1999.
(32) Sprenger, M.; Walheim, S.; Budkowski, A.; Steiner, U. *Interface Sci.* **2003**, *11*, 225.
(33) Bernasik, A.; Rysz, J.; Budkowski, A.; Kowalski, K.; Camra, J.; Jedliński, J. *Macromol. Rapid Commun.* **2001**, *22*, 829−834.
(34) Nauman, E. B.; He, D. Q. *Polymer* **1994**, *35*, 2243.
(35) Binder, K. *Adv. Polym. Sci.* **1999**, *138*, 1.
(36) Elbs, H.; Funkunaga, K.; Stadler, R.; Sauer, G.; Magerle, R.; Krausch, G. *Macromolecules* **1999**, *32*, 1204.
(37) Lawrence, C. J. *Phys. Fluids* **1988**, *31*, 2786.
(38) Schubert, D. W. *Polym. Bull. (Berlin)* **1997**, *38*, 177.
(39) Extrand, C. W. *Polym. Eng. Sci.* **1994**, *34*, 390.
(40) Walheim, S. Ph.D. Thesis, University of Konstanz, 2000.
(41) Tanaka, H. *Phys. Rev. Lett.* **1990**, *65*, 3136.
(42) Lookman, T.; Wu, Y.; Alexander, F. J. *Phys. Rev. E* **1996**, *53*, 5513.
(43) Gutmann, J. S.; Müller-Buschbaum, P.; Stamm, M. *Faraday Discuss.* **1999**, *112*, 258 and references therein.
(44) Walheim, S.; Böltau, M.; Mlynek, J.; Krausch, G.; Steiner, U. *Macromolecules* **1997**, *30*, 4995.
(45) Tanaka, H. *Phys. Rev. E* **1995**, *51*, 1313.
(46) Ton-That, C.; Shard, A. G.; Teare, D. O. H.; Bradley, R. H. *Polymer* **2001**, *42*, 1121.
(47) Ton-That, C.; Shard, A. G.; Teare, D. O. H.; Bradley, R. H. *Polymer* **2002**, *43*, 4973.
(48) de Gennes, P. G. *Eur. Phys. J. E* **2001**, *6*, 421.
(49) Mitov, Z.; Kumacheva, E. *Phys. Rev. Lett.* **1998**, *81*, 3427.
(50) Tanaka, K.; Takahara, A.; Kajiyama, T. *Macromolecules* **1996**, *29*, 3232.
(51) Dalnoki-Veress, K.; Forrest, J. A.; Stevens, J. R.; Dutcher, J. R. *J. Polym. Sci., Part B: Polym. Phys.* **1996**, *34*, 3017.
(52) Affrossman, S.; Henn, G.; O'Neill, S. A.; Pethrick, R. A.; Stamm, M. *Macromolecules* **1996**, *29*, 5010.
(53) The morphologies similar to that recorded for longer drying times (thicker films) were obtained in the films spin-cast more rapidly and additionally annealed.[22]
(54) Jukes, P. C.; Heriot, S. Y.; Sharp, J. S.; Jones, R. A. L. *Macromolecules* **2005**, *38*, 2030.
(55) Tanaka, H. *Phys. Rev. E* **1996**, *54*, 1709.
(56) Wang, H.; Composto, J. *Phys. Rev. E* **2000**, *61*, 1659.
(57) Rysz, J.; Ermer, H.; Budkowski, A.; Bernasik, A.; Lekki, J.; Juengst, G.; Brenn, R.; Kowalski, K.; Camra, J.; Lekka, M.; Jedliński, J. *Eur. Phys. J. E* **2001**, *5*, 207.
(58) Binder, K. *J. Chem. Phys.* **1983**, *79*, 6387.
(59) Brochard Wyart, F.; Daillant, J. *Can. J. Phys.* **1990**, *68*, 1084.

MA051242S